

ARTICLE OPEN



Key to ENSO phase-locking simulation: effects of sea surface temperature diurnal amplitude

Xiaodan Yang^{1,2,3}, Ying Bao^{1,2,3}, Zhenya Song^{1,2,3} , Qi Shu^{1,2,3} , Yajuan Song^{1,2,3}, Xin Wang^{4,5,6}  and Fangli Qiao^{1,2,3} 

The tendency of El Niño/Southern Oscillation (ENSO) events to peak during boreal winter is known as ENSO phase-locking, whose accurate simulation is essential for ENSO prediction. However, the simulated peaks of ENSO events usually occur outside boreal winter in state-of-the-art climate models. Based on the Coupled Model Intercomparison Project Phase 6 (CMIP6) models, the model with a more reasonable diurnal amplitude (DA) in the sea surface temperature (SST) had a better simulation ability for ENSO phase-locking compared with other models. Further experiments based on the earth system model revealed that the DA is vital for ENSO phase-locking simulation primarily due to the spatial inhomogeneities in seasonal DA anomaly variations in ENSO years with positive/negative DA anomalies in the central equatorial Pacific and negative/positive in the western or eastern Pacific during El Niño/La Niña. Our findings indicate that DA simulation in climate models is crucial for resolving the long-standing failure associated with the ENSO phase-locking simulation accuracy.

npj Climate and Atmospheric Science (2023)6:159; <https://doi.org/10.1038/s41612-023-00483-3>

INTRODUCTION

The El Niño/Southern Oscillation (ENSO) is the most consequential mode of climate variability on earth and has enormous impacts on global ecosystems, agriculture, and extreme weather^{1–5}. ENSO events initiate during boreal spring and summer, peak during boreal winter, and decay in the following spring—a phenomenon known as ENSO phase-locking. Accurate ENSO simulation, including its spatial and temporal characteristics, remains a challenge^{6,7}. Particularly, most climate models cannot realistically simulate ENSO phase-locking because of the biases in the mean state and annual cycle in tropical climates^{8,9}. Such failure in ENSO phase-locking simulations limits predictability and reduces the forecast ability of ENSO, i.e., the “spring barrier” in ENSO forecasts, and even affects the modeling of the global climate system through pantropical climate interactions^{10–12}. Therefore, reasonable ENSO phase-locking simulation is consequential to climate models.

Resolving diurnal variations in sea surface temperature (SST) caused by solar radiation and the earth’s rotation can impact ENSO simulations, including its amplitude, frequency, and asymmetry, based on studies in which the air-sea coupling frequency is improved from daily to 3 h or higher^{13–16}. However, the diurnal amplitude (DA) of the SST (the daily maximum SST minus the daily minimum SST), which can exceed 3 °C under calm and clear conditions^{17–19}, is underestimated in previous studies because capturing 90% of the DA requires a thickness of approximately 1 m in the upper ocean layer to resolve the shoaling boundary layer during the daytime^{20,21}. As well as improving vertical resolution, diurnal variation parameterization schemes that ignore full mixed-layer dynamics processes can simulate the accurate DA of near-surface temperatures^{17,22,23}. However, owing to their resulting high computation and storage requirements with high vertical resolution in the upper ocean or the rare use of parameterization schemes in previous studies, the

influence of accurate DA simulation on ENSO phase-locking simulation in climate models remains unexplored.

In this study, we demonstrate that climate models, which simulate a large DA in the SST close to observations in the equatorial Pacific region, could considerably simulate ENSO phase-locking, by using outputs from the Coupled Model Intercomparison Project Phase 6 (CMIP6). Moreover, we explored the underlying dynamics of ENSO phase-locking using simulations with large or small DAs from the second version of the First Institute of Oceanography Earth System Model (FIO-ESM v2.0)²⁴. Our results suggest that realistically simulating the SST DA in the climate model is necessary to accurately simulate ENSO phase-locking.

RESULTS

Comparisons of simulated ENSO phase-locking with large and small DAs

The impact of daily variation on mean SST is more pronounced in experiments with a large DA than those with a small DA (Supplementary Fig. 1). It is because a large DA experiment captures stronger daily warming than that in a small DA experiment, while nocturnal cooling is similar in both types of experiments. Under calm conditions and strong solar radiation during the daytime, the mixed layer depth can be shallow, which can only be simulated reasonably in large DA experiments with high vertical resolution or a diurnal parameterization scheme. However, the nocturnal minimum (the bulk mixed layer temperature) can be the same in both the large and small DA experiments due to deep mixed layer depths with wind stress mixing and convection at nighttime. Therefore, the daily-mean SST is more likely to be modified in the large DA experiments²⁵ with reasonable daily warming simulation (Supplementary Fig. 1). Moreover, the large DA experiment may affect the ENSO phase-

¹First Institute of Oceanography and Key Laboratory of Marine Science and Numerical Modeling, Ministry of Natural Resources, Qingdao, China. ²Laoshan Laboratory, Qingdao, China. ³Shandong Key Laboratory of Marine Science and Numerical Modeling, Qingdao, China. ⁴State Key Laboratory of Tropical Oceanography, South China Sea Institute of Oceanology, Chinese Academy of Sciences, Guangzhou, China. ⁵Global Ocean and Climate Research Center, South China Sea Institute of Oceanology, Chinese Academy of Sciences, Guangzhou, China. ⁶Innovation Academy of South China Sea Ecology and Environmental Engineering, Chinese Academy of Sciences, Guangzhou, China.

[✉]email: songroy@fio.org.cn; wangxin@scsio.ac.cn; qiaofl@fio.org.cn

locking simulation more than the small DA experiment after modifying the mean SST.

Here, we quantitatively evaluated the impact of DA on ENSO phase-locking simulations by assessing the abilities of CMIP6 models with different DA simulation skills to reproduce ENSO phase-locking in their historical simulations between 1850 and 2014, and comparing it with commonly used observations, such as the Hadley Center Sea Ice and Sea Surface Temperature (HadISST)²⁶ and Extended Reconstructed Sea Surface Temperature (ERSST) version 5 datasets²⁷. To maintain consistent data lengths, we selected all periods between 1870 and 2014. Thirty-five CMIP6 models with high air-sea coupling frequencies of approximately 3 h were divided into two groups. Models with a high vertical resolution of 2 m or higher in the upper ocean or using a diurnal variation parameterization scheme in the ocean model were treated as simulating large DAs. Others with a low vertical resolution were treated as simulating small DAs (Supplementary Table 1).

A histogram of peak ENSO events derived from the Niño 3.4 index is an effective method for characterizing ENSO phase-locking behavior²⁸. Histograms of the observational data confirmed that ENSO events tend to peak between November and January (Fig. 1a, b). Furthermore, CMIP6 models with large DA showed a greater probability of ENSO peaking in boreal winter than those with small DA, even though the improvement during El Niño appears to be more remarkable than that during La Niña (Fig. 1c, d). Moreover, the preferred month (the calendar month at which the histogram has its maximum peak) and preferred strength (see ENSO's phase-locking preference strength in Methods) can be used to evaluate the characteristics of ENSO phase-locking²⁹. In CMIP6 models with small DAs, only 75% (15 out of 20 models) and 60% (12 out of 20 models) of the models have preferred months that fell within boreal winter during El Niño and La Niña events, respectively, with weak preferred strengths (Supplementary Fig 2a, c, e, g). In contrast, in models with large DAs, the preferred months were all in boreal winter for El Niño and La Niña events (15 out of 15 models), with strongly preferred strengths close to observations (Supplementary Fig. 2b, d, f, h).

In addition to analyzing the CMIP6 model outputs, we investigated the influences of DAs on the ENSO phase-locking simulation by comparing the outputs of simulations based on FIO-ESM v2.0 with large DAs (with the diurnal variation parameterization scheme, which could simulate large DAs of SST, called Exp_large_DA) to those with small DAs (without the parameterization scheme, which could only simulate small DAs of SST with the coarse vertical resolution, called Exp_small_DA). In Exp_large_DA, even though the probabilities during El Niño are overestimated in December but underestimated in November, the probabilities of ENSO peaking in the boreal winter were considerably higher than those in Exp_small_DA during El Niño and La Niña events (Fig. 1e, f), consistent with those in the CMIP6 outputs. This comparison supports the hypothesis that SST DA simulation is essential for realistically simulating ENSO phase-locking in climate models.

Accurate SST anomaly tendencies during ENSO contribute to reasonable ENSO phase-locking

Next, we evaluated the impact of accurate DA simulations on simulating ENSO phase-locking by influencing the SST anomaly (SSTA) tendencies—the rates of variations of the SSTAs in the ENSO events—because they may lead to the failure of the models to reasonably simulate ENSO phase-locking by incorrectly simulating the preferred month or by underestimating the preferred strength^{5,30}.

First, ENSO events can be divided into three phases. The phase between January and July is defined as the onset phase in this study, representing the phase before ENSO develops. Additionally, ENSO mainly develops between August and December,

considered the developing phase. Moreover, ENSO decays between January and May of the following year, designated the decaying phase. Notably, the SSTA tendencies in CMIP6 models with large DA were broadly consistent with observations in all three phases (Fig. 2c, d); however, those in models with small DAs had large discrepancies during El Niño and La Niña events (Fig. 2a, b), indicating incorrect physical processes during ENSO events.

The mean biases in the SSTA tendencies in models with large DAs were significantly lower than those with small DAs in the onset and developing phases during El Niño events (Fig. 2e). Furthermore, in the decaying phase, even though the mean biases were slightly higher in models with large DAs than in those with small DAs when compared with HadISST, they were still lower when compared with ERSST. Moreover, during La Niña events, the mean biases in the SSTA tendencies were effectively reduced in the CMIP6 models with large DAs, especially in the onset and decaying phases (Fig. 2f). However, during the developing phase, the mean SSTA tendencies in the models with small DAs appeared to be more consistent with the observations than those in the models with large DAs. This consistency can be explained by some of the inappropriate positive SSTA tendencies during this period in models with small DA (Fig. 2b).

In general, SSTA tendencies are more accurate in models with large DAs than those with small DA during El Niño and La Niña events, further contributing to the precise simulation of winter phase-locking. To illustrate the SST DA roles on SSTA tendencies during ENSO and clarify the intrinsic mechanism, the dynamics processes are compared between the Exp_large_DA (with the diurnal variation parameterization scheme, which could simulate large DAs of SST) and Exp_small_DA (without the parameterization scheme, which could only simulate small DAs of SST with the coarse vertical resolution) experiments using FIO-ESM v2.0 next.

Exploring oceanic processes that influence SSTA tendencies via mixed-layer heat budget analysis

During El Niño, the SSTA tendency decreased during the onset phase but increased during the developing phase in Exp_large_DA compared with Exp_small_DA (Fig. 3a), consistent with the pattern in the CMIP6 models (Fig. 2e). Variation in the SSTA tendencies inhibits the previously developed El Niño, and then forces El Niño to mature during the developing phase. Furthermore, the negative SSTA tendency in the decaying phase was enhanced, which benefits El Niño decay from its peak in boreal winter. This situation was qualitatively similar for La Niña, except that the signs of all terms were reversed (Fig. 3b). Therefore, the difference in SSTA tendencies between Exp_large_DA and Exp_small_DA is the main reason for the difference in ENSO phase-locking simulations.

Furthermore, we elucidated the dynamics underlying SST DA simulation effects on the accuracy of SSTA tendency simulation during ENSO by applying a mixed-layer heat budget analysis to the Niño 3.4 region (170°–120°W, 5°S–5°N), verified to be conserved in the heat budget in this region. This is because the SSTA tendencies estimated using the analysis method were consistent with the actual value (Supplementary Fig. 3). The heat budget analysis elucidates the contribution of the key feedbacks that determine the SSTA tendency of ENSO, including the mean horizontal dynamical heating term (MH), thermocline feedback (TH), zonal advective feedback (ZA), meridional advective feedback (MA), Ekman pumping feedback (EK), nonlinear advective dynamic heating (NDH), and thermodynamic damping (TD)³⁰ (Supplementary Figs 4, 5). Additionally, the mean vertical temperature above 50 m, set as the mixed layer depth, was treated as a proxy for SST. Furthermore, the comparison between the Exp_large_DA and Exp_small_DA experiments revealed that the differences (Δ) in ZA, MH, and MA (Fig. 3c, d) are the main

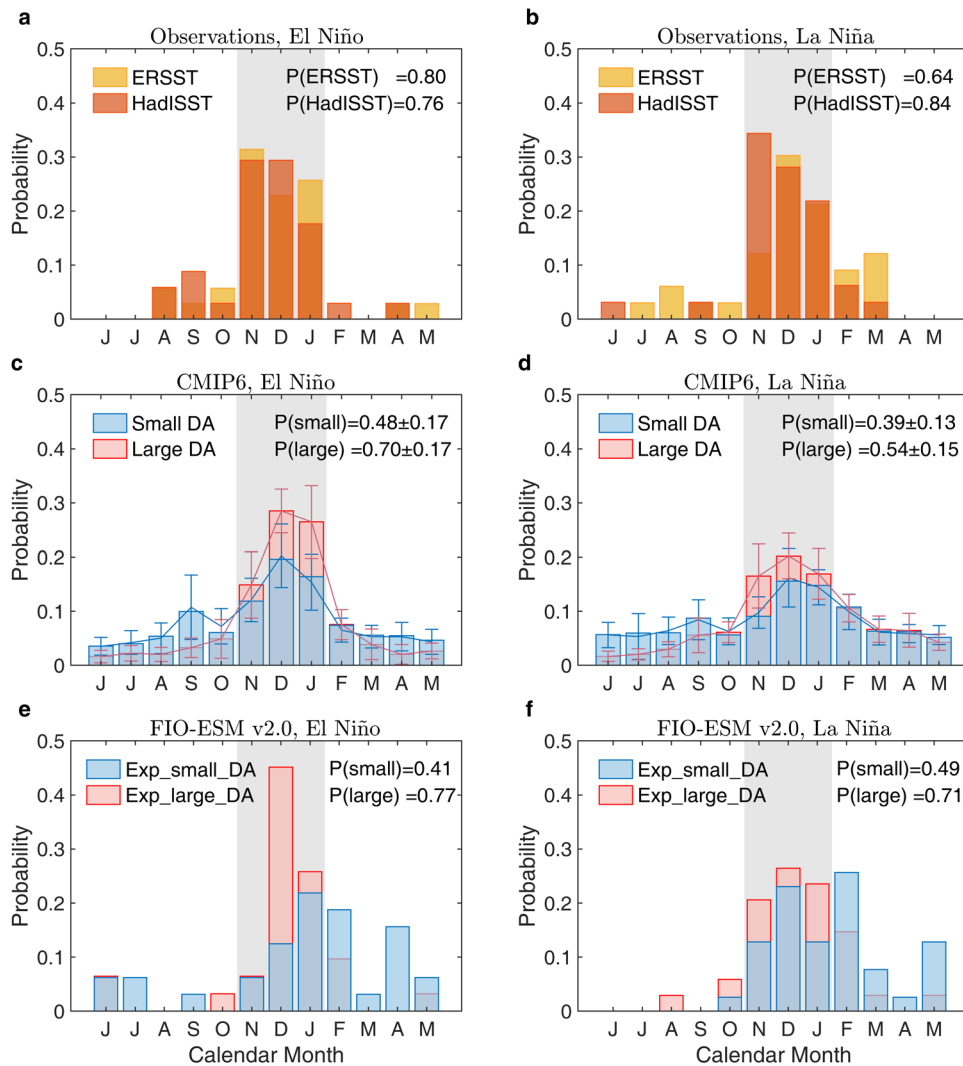


Fig. 1 Peak phase histograms depicting ENSO phase-locking. **a, b** Probabilities of peak months during El Niño (**a**) and La Niña (**b**) in observations. **c, d**, Same as (**a, b**), but for the ensemble mean of the CMIP6 models with large or small DA in the upper ocean during El Niño (**c**) and La Niña (**d**). Standard errors of the mean represent the 95% confidence intervals from all related ENSO events. **e, f** Similar to (**c, d**), but using FIO-ESM v2.0 Exp_small_DA and Exp_large_DA experiment results. The summed probabilities of peak times that occur in boreal winter (gray band) are given at the top right of each panel. The CMIP6 ensemble-wise standard deviation value of P is provided in (**c, d**).

reasons affecting the SSTA tendencies (Fig. 3a, b) during El Niño and La Niña events.

Additionally, after decomposing ΔZA , ΔMH , and ΔMA into different terms (see Decomposing ΔZA , ΔMH , and ΔMA into different terms and exploring the key processes in Methods), we found that the difference in the horizontal oceanic current anomalies ($\Delta u'$ and $\Delta v'$), and the difference in the meridional gradient of the SSTAs ($\Delta \frac{\partial T}{\partial y}$), are the key processes contributing to the variation in SSTA tendencies (Supplementary Fig. 6), which further impacts ENSO phase-locking. Moreover, $\Delta u'$ and $\Delta v'$ between the Exp_large_DA and Exp_small_DA experiments were related to the difference in zonal wind anomalies (ZWAs). Furthermore, the difference in ZWAs was mainly associated with the difference in SSTAs through air-sea interactions (Fig. 4a, b). Thus, the air-sea interactions in ENSO events are discussed next.

Air-sea interactions in ENSO events initiated by differences in SSTA

The difference in SSTAs between the Exp_large_DA and Exp_small_DA experiments involved complicated air-sea

interactions, including multi-feedback processes, has been obtained (Fig. 4a, b). The spatial inhomogeneities in SSTA differences among the western equatorial Pacific (WP), central equatorial Pacific (CP), and eastern equatorial Pacific (EP) could lead to ZWA differences, which could further weaken or amplify SSTA differences through air-sea interactions (Fig. 4a, b). First, during the El Niño (La Niña) event, the negative (positive) zonal gradient of the SSTA difference in the EP and CP between March and June increased (decreased) the easterly ZWA in the Niño 3.4 region, thereby enhancing the negative (positive) zonal gradient of the SSTA difference via the Bjerknes feedback³¹. Next, the positive (negative) zonal gradient of the SSTA difference in the CP and WP between August and December weakens (strengthens) the easterly ZWA, thereby increasing the positive (negative) zonal gradient of the SSTA difference. Lastly, the negative (positive) zonal gradient of the SSTA difference in the EP and CP between January and May of the following year strengthens (weakens) the easterly ZWA, further strengthening the negative (positive) zonal gradient of the SSTA difference, similar to the previous year. Additionally, the differences in the ZWA associated with zonal SSTA gradient contributed to $\Delta u'$ between the Exp_large_DA and

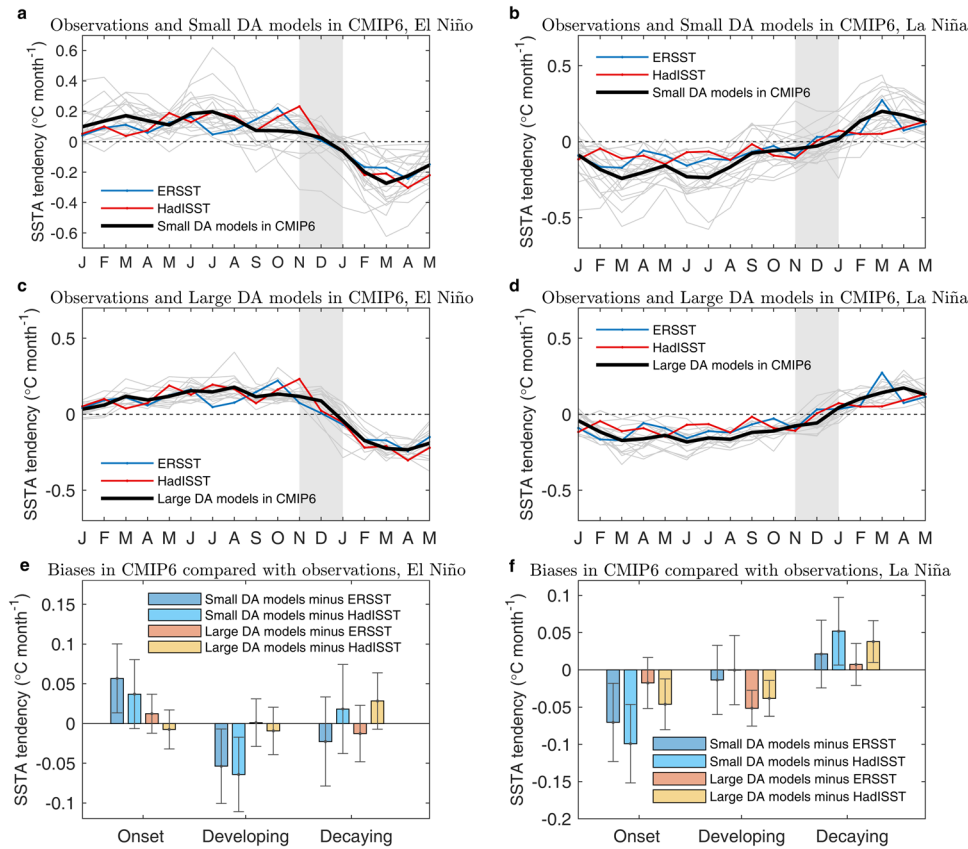


Fig. 2 SSTA tendencies during ENSO events. **a, b** SSTA tendencies in observations and Small DA models in CMIP6 during El Niño (**a**) and La Niña events (**b**). Thin gray lines are the tendencies in each CMIP6 model, and the thick black line represents the ensemble mean. **c, d** Same as (**a, b**), but for Large DA models in CMIP6. **e, f** Biases in the mean SSTA tendencies in CMIP6 models compared with observations during El Niño (**e**) and La Niña events (**f**). Standard errors of the mean represent the 95% confidence intervals. The gray bands in (**a–d**) represent boreal winter.

Exp_small_DA experiments (Supplementary Figs. 6b, h). Overall, $\Delta u'$ causes variations in ZA, thereby influencing the difference in SSTA tendencies and affecting the improvement in the ENSO phase-locking simulations.

Besides $\Delta u'$, the differences in the ZWA in the equatorial region also influence variations in $\Delta v'$ via Sverdrup transport, which is affected by the vorticity (stretching) imposed by the wind stress curl^{4,32}. Between March and May, during El Niño (La Niña) event, the divergence (convergence) of $\Delta v'$ was associated with the strengthening (weakening) of the easterly ZWA. In contrast, between August and November, the convergence (divergence) of $\Delta v'$ was related to the weakening (strengthening) of the easterly ZWA (Supplementary Figs. 6d, j). Furthermore, the $\Delta v'$ contributes to the difference in MA, which influences ENSO phase-locking simulation by affecting the SSTA tendencies.

Moreover, the difference in SSTAs in the equatorial Pacific region could also lead to a difference in the meridional SSTA gradient ($\Delta \frac{\partial T'}{\partial y}$) (Supplementary Figs. 6f, l). For example, in the developing phase during the El Niño event and the onset and decaying phases during the La Niña event, the positive SSTA difference near the equatorial region caused a negative (positive) $\Delta \frac{\partial T'}{\partial y}$ in the Northern (Southern) Hemisphere. In contrast, the negative SSTA difference caused the opposite $\Delta \frac{\partial T'}{\partial y}$, such as in the onset and decaying phases during the El Niño event and the developing phase during the La Niña event. Overall, variations in $\Delta \frac{\partial T'}{\partial y}$ could lead to a difference in MH, thereby contributing to SSTA tendencies and impacting the ENSO phase-locking simulation.

Spatial inhomogeneities in seasonal variation in DA contribute to SSTA difference

The reasons for the SSTA differences between the Exp_large_DA and Exp_small_DA experiments are explored next. We discovered that the differences in SSTAs were consistent with differences in DAAs between the Exp_large_DA and Exp_small_DA experiments (Fig. 4c, d), which perfectly match the seasonal variation in DAA in the Exp_large_DA experiment (figure not shown), indicating that the variation in SSTA difference is associated with the variation in DAA in ENSO years^{33,34}.

As discussed previously in ref. ³⁴, the seasonal variations in DAA among the WP, CP, and EP regions are not synchronous in the years ENSO events occur. Notably, DAA in the CP becomes positive (negative) approximately one year before El Niño (La Niña) events and reaches a maximum between August and September, approximately 3 to 4 months before the mature ENSO phase. Furthermore, between November and February, the negative (positive) DAA in the EP was relatively strong, consistent with the mature phase of El Niño (La Niña) events. Additionally, the variations in DAA in the CP and EP regions in ENSO years are controlled by the combined effects of solar radiation, wind speed, and latent heat fluxes³⁴. Moreover, we found that the DAA was negative (positive) between January and March in the EP region and April and September in the WP region during El Niño (La Niña) events. This pattern may also be associated with variations in atmospheric factors; however, this suggestion requires further verification.

We found that the spatial inhomogeneities in seasonal DAA variations among the WP, CP, and EP regions in the equatorial Pacific in years in which ENSO events occurred are the principal

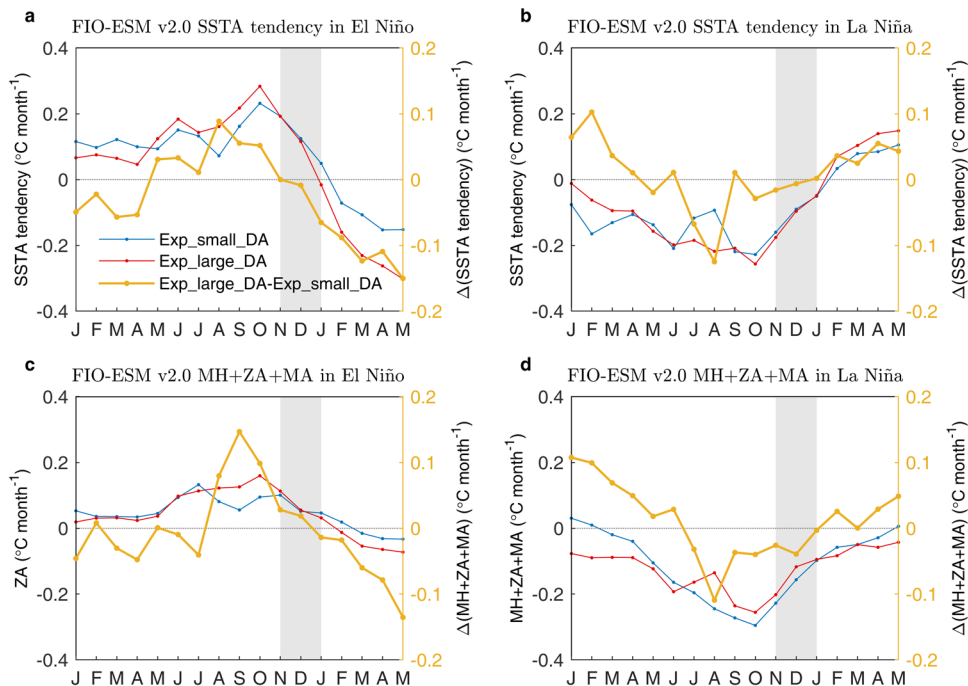


Fig. 3 Difference in SSTA tendencies between the Exp_large_DA and Exp_small_DA experiments in the FIO-ESM v2.0 model. **a, b** SSTA tendencies in Exp_small_DA (blue line) and Exp_large_DA (red line) experiments during El Niño (**a**) and La Niña (**b**). The difference between the Exp_large_DA and Exp_small_DA experiment results (yellow line) uses the scale on the right vertical axis. **c, d** Same as (**a, b**), but for the combined MH, ZA, and MA processes during El Niño (**c**) and La Niña (**d**), respectively. The gray bands represent boreal winter.

contributors to the reasonable ENSO phase-locking simulation (Fig. 5). First, the spatial inhomogeneities in seasonal variations in DAA lead to the spatial inhomogeneities in seasonal variations in the SSTA differences. Furthermore, the SSTA difference gradients among the WP, CP, and EP regions promoted equatorial ZWA differences. For example, in the onset/decaying (developing) phase during El Niño, the negative (positive) gradient between the EP and CP (CP and WP) SSTA differences increased (decreased) the easterly ZWA. Moreover, these effects were amplified via the Bjerknes feedback. Next, the strengthening (weakening) of the easterly ZWA increases (decreases) $\Delta u'$ and leads to the divergence (convergence) of $\Delta v'$ above the mixed layer depth. Furthermore, the negative (positive) SSTA difference in the Niño 3.4 region caused variations in $\Delta \frac{\partial T}{\partial y}$. Additionally, these differences contribute to the decrease (increase) in oceanic processes related to SSTA tendencies in the onset/decaying (developing) phase, such as ZA, MA, and MH. Thereby, the SSTA tendencies decrease (increase) in the onset/decaying (developing) phase during El Niño events. Notably, the situation was qualitatively similar during La Niña, but all of the terms were sign-reversed. Lastly, the precision of the ENSO phase-locking simulation was enhanced after improved SSTA tendencies.

DISCUSSION

We found that approximately half of the CMIP6 models (15/35) with large DA simulate a significantly larger probability of ENSO events peaking in boreal winter than those with small DA. However, climate models with different SST DA simulation skills differ in many other ways, such as horizontal resolutions, physical processes, and parameterizations of vertical turbulent mixing. Therefore, future studies based on an enlarged climate model ensemble with a large DA, with a design similar to that of climate models with a small DA, could comprehensively assess the role of accurate DA in ENSO phase-locking simulation.

Our FIO-ESM v2.0 experiments with or without a diurnal variation parameterization scheme have confirmed the

importance of accurate DAs in ENSO phase-locking simulation primarily due to the spatial inhomogeneities in seasonal DAA variations in ENSO years. Furthermore, besides phase-locking, other characteristics of ENSO, such as amplitude, period, and skewness, also partially improved after including accurate DAs in FIO-ESM v2.0; however, the mechanism driving this relationship remains unknown and requires further examination. Therefore, we suggest that an accurate DA simulation in climate models is crucial for improving the ENSO phase-locking simulation and understanding the ENSO phenomenon.

METHODS

CMIP6 simulations

We analyzed the historical simulations from 35 CMIP6 models with air-sea coupling frequencies of approximately 3 h or better, including FIO-ESM v2.0, for the monthly SST fields (labeled “tos” in the data archives) between 1870 and 2014. We interpolated the SST with different resolutions to a regular $1^\circ \times 1^\circ$ longitude-latitude grid.

FIO-ESM v2.0 experiments

FIO-ESM v2.0 is a fully coupled earth system model with ocean, atmosphere, land surface, sea ice, and ocean surface wave models²⁴. Diurnal variation in the SST was demonstrated by incorporating the diurnal variation parameterization scheme²² into the ocean component model. Furthermore, using the parameterization scheme (Exp_large_DA), the SST near the ocean surface can be diagnosed, realistically simulating the SST DA. Moreover, regarding the experiment conducted without the parameterization scheme (Exp_small_DA), the model had 60 vertical levels, and the surface layer was 10 m thick. Therefore, SST refers to the mean seawater temperature of the 10 m water column, which can barely resolve the SST DA used in the air-sea interaction. Regarding the experiment using the parameterization scheme, the model had 61 vertical levels with diagnosed SST in

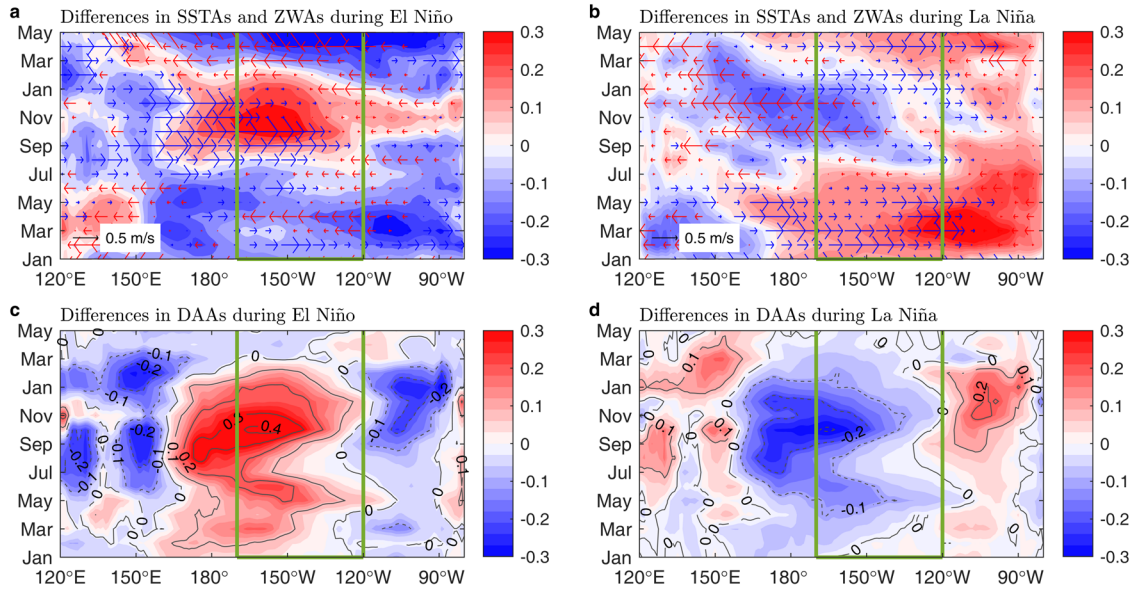


Fig. 4 Effect of SST DA on SSTA and ZWA during ENSO events. **a, b** Differences in SSTA (blue to red coloring) and ZWA (arrows) between Exp_large_DA and Exp_small_DA experiments during El Niño (**a**) and La Niña (**b**) in the FIO-ESM v2.0 model. **c, d** Similar to (**a, b**), but for differences in DAAs. The values are averaged between 5°S and 5°N. The green squares represent the Niño 3.4 region.

the first level, which the coupler relays to calculate the air-sea heat flux. Notably, the atmospheric and ocean component models exchange data with the coupler at 30 min and 3 h intervals, respectively. The high coupling frequency contributed to the diurnal variation in the model. Furthermore, all of the forcing data of the two experiments are set to the observation data between 1850 and 2014 for the historical run that followed the protocols defined by CMIP6³⁵.

SST datasets

The SST datasets referred to as observations were derived from the HadISST dataset between 1870 and 2021 on a $1^\circ \times 1^\circ$ grid²⁶ and ERSST version 5 between 1854 and 2022 on a $2^\circ \times 2^\circ$ grid²⁷. We selected the periods between 1870 and 2014 to maintain consistent data lengths with the CMIP6 model data.

Definitions of the indices

ENSO events in the observations and models were defined as the intervals in the Niño 3.4 index that exceeded $\pm 0.5^\circ\text{C}$ for at least five consecutive months after a 3-month running average was applied. Additionally, the Niño 3.4 index is defined as the detrended monthly SST anomalies in the Niño 3.4 region ($170^\circ\text{--}120^\circ\text{W}$, $5^\circ\text{S--}5^\circ\text{N}$). The anomalies were based on the climatology of each period in the dataset.

ENSO's phase-locking preference strength

The metric for the strength of the ENSO phase-locking preference (φ_s) is defined as follows²⁹:

$$\varphi_s = \frac{4}{3} \left(\varphi_{\max} - \frac{1}{4} \right) \quad (1)$$

where φ_{\max} indicates the sum of the 3-month highest histogram values centered on the preferred month.

Mixed layer heat budget analysis

Following previous studies^{30,36}, the mixed layer depth was set to 50 m for the Niño 3.4 region in this study. The heat budget above

the mixed layer depth can be derived as follows³⁰:

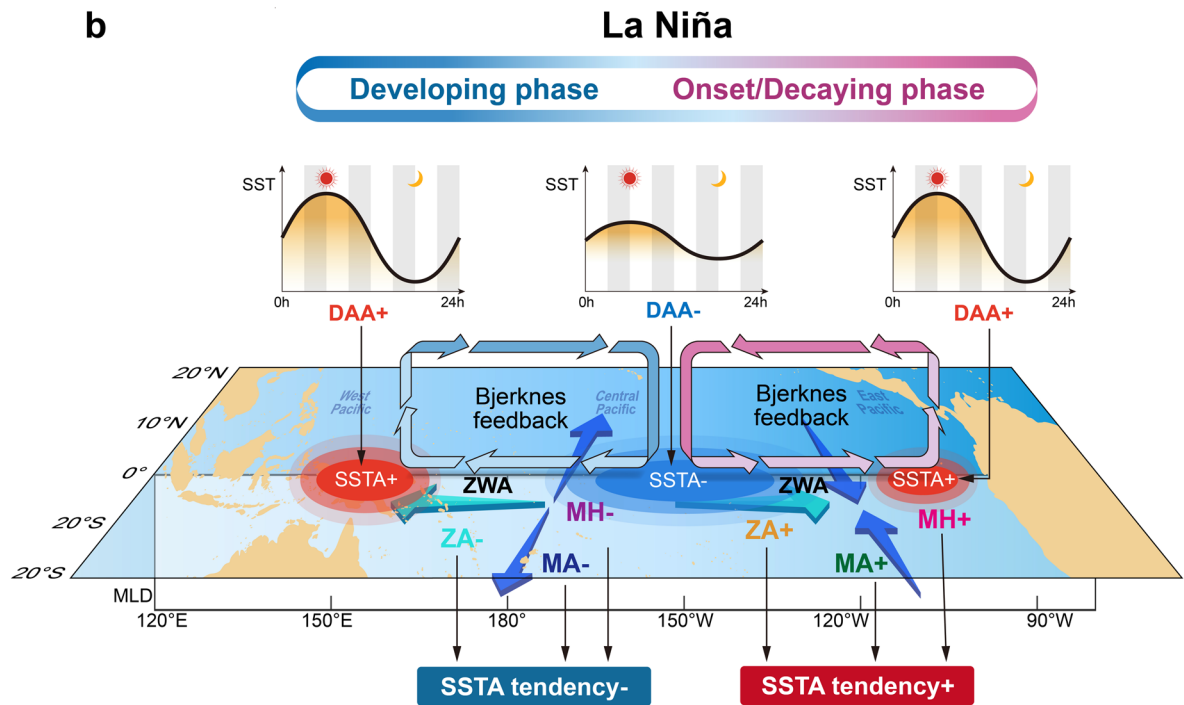
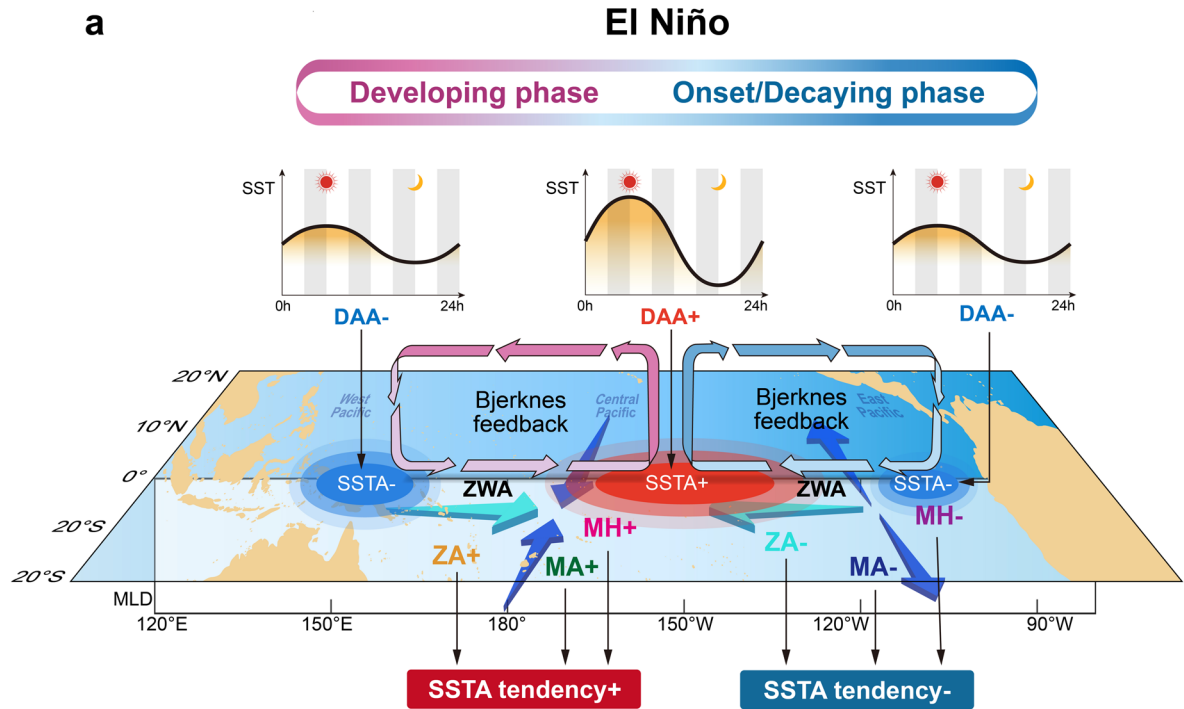
$$\frac{\partial T'}{\partial t} = - \underbrace{\left(\bar{u} \frac{\partial T'}{\partial x} + \bar{v} \frac{\partial T'}{\partial y} \right)}_{\text{MH}} - \underbrace{\bar{w} \frac{\partial T'}{\partial z}}_{\text{TH}} - \underbrace{u' \frac{\partial \bar{T}}{\partial x}}_{\text{ZA}} - \underbrace{v' \frac{\partial \bar{T}}{\partial y}}_{\text{MA}} - \underbrace{w' \frac{\partial \bar{T}}{\partial z}}_{\text{EK}} - \underbrace{\left(u' \frac{\partial T'}{\partial x} + v' \frac{\partial T'}{\partial y} + w' \frac{\partial T'}{\partial z} \right)}_{\text{NDH}} + \underbrace{Q'}_{\text{TD}} + \underbrace{\text{Res}}_{\text{Residual}} \quad (2)$$

where T indicates the ocean potential temperature; u , v , and w represent the zonal, meridional, and vertical ocean currents, respectively; the primes and overbars denote the anomalies during ENSO events and the climatological monthly mean, respectively; and Q , ρ , C_p , and H are the surface heat flux, density of seawater, seawater specific heat, and depth of the mixed layer, respectively. Additionally, the terms on the right side of the equation represent the mean horizontal dynamical heating term (MH), thermocline feedback (TH), zonal advective feedback (ZA), meridional advective feedback (MA), Ekman feedback (EK), non-linear advection (NDH), thermal damping by net sea surface heat flux (TD) and the residual term.

Decomposing ΔZA , ΔMH , and ΔMA into different terms and exploring the key processes

The difference in ZA ($-\Delta(u' \frac{\partial \bar{T}}{\partial x})$) between the Exp_large_DA and Exp_small_DA experiments can be decomposed into three terms, namely, $-u' \Delta \frac{\partial \bar{T}}{\partial x}$, $-\Delta u' \frac{\partial \bar{T}}{\partial x}$, and $-\Delta u' \Delta \frac{\partial \bar{T}}{\partial x}$, where u' and $\frac{\partial \bar{T}}{\partial x}$ denote the ENSO-related zonal oceanic current anomalies and zonal gradients in the mean-state SST, respectively. Moreover, from the Supplementary Figs. 6a, g, we can conclude that $-\Delta u' \frac{\partial \bar{T}}{\partial x}$ is the key process responsible for ZA variation during El Niño and La Niña. As the zonal gradient of the mean-state SST ($\frac{\partial \bar{T}}{\partial x}$) is always negative, the variation in the ENSO-related westward zonal oceanic current anomalies ($-\Delta u'$) primarily causes the positive and negative conversions in the ZA difference between the Exp_large_DA and Exp_small_DA experiments (Supplementary Fig. 6b, d).

Furthermore, the difference in MA ($-\Delta(v' \frac{\partial \bar{T}}{\partial y})$) between the Exp_large_DA and Exp_small_DA experiments can be decomposed into three terms, namely, $-v' \Delta \frac{\partial \bar{T}}{\partial y}$, $-\Delta v' \frac{\partial \bar{T}}{\partial y}$, and $-\Delta v' \Delta \frac{\partial \bar{T}}{\partial y}$,



- | | | | | | |
|------------|--|-------------|----------------------------------|----------|--------------------|
| | Zonal ocean current anomaly | | Meridional ocean current anomaly | | Wind speed anomaly |
| DAA | Diurnal amplitude anomaly | SSTA | Sea surface temperature anomaly | + | Increase |
| ZA | Zonal advective feedback | MA | Meridional advective feedback | - | Decrease |
| MH | Mean horizontal dynamical heating term | | | | |

where v' and $\frac{\partial \bar{T}}{\partial y}$ denote the ENSO-related meridional oceanic current anomalies and meridional gradients of the mean-state SST, respectively. ΔMA is mainly represented by the $-\Delta v' \frac{\partial \bar{T}}{\partial y}$ term

(Supplementary Fig. 6c, i). Additionally, the variation in the positive and negative conversions in the MA difference was caused by the variation in the ENSO-related meridional oceanic current anomalies ($-\Delta v'$) because the sign of the meridional

Fig. 5 Schematic diagram of the influence of DA on ENSO phase-locking. **a, b** The differences between Exp_large_DA and Exp_small_DA experiment results during El Niño (**a**) and La Niña (**b**). SST with different diurnal amplitudes in the onset/decaying and developing phases are represented (black lines). The red and blue ovals indicate the SSTA differences in the equatorial Pacific. The plus (+) and minus (−) represent the increase and decrease of the DAA, SSTA, and oceanic processes (ZA, MA, and MH), respectively. Pink and blue-grey arrows represent the equatorial ZWA differences promoted by the SSTA difference gradients among the WP, CP, and EP regions, and the Bjerknes feedback processes are given in the figure. Cyan and blue arrows indicate the zonal and meridional ocean current anomalies, respectively. MLD represents the mixed layer depth at 50 m.

gradient in the mean-state SST ($\frac{\partial \bar{T}}{\partial y}$) remained unchanged within this period.

Next, the difference in MH ($-\Delta(\bar{u}\frac{\partial T'}{\partial x} + \bar{v}\frac{\partial T'}{\partial y})$) between the Exp_large_DA and Exp_small_DA experiments comprises $-\Delta(\bar{u}\frac{\partial T'}{\partial x})$ and $-\Delta(\bar{v}\frac{\partial T'}{\partial y})$, where \bar{u} and \bar{v} represent the mean-state zonal and meridional currents, respectively, and $\frac{\partial T'}{\partial x}$ and $\frac{\partial T'}{\partial y}$ denote the zonal and meridional gradients of the ENSO-related SST anomalies, respectively, of which $-\Delta(\bar{v}\frac{\partial T'}{\partial y})$ plays a dominant role in influencing Δ MH (Supplementary Fig. 6e, k). Moreover, $-\Delta(\bar{v}\frac{\partial T'}{\partial y})$ can be decomposed into three terms: $-\bar{v}\Delta\frac{\partial T'}{\partial y}$, $-\Delta\bar{v}\frac{\partial T'}{\partial y}$, and $-\Delta\bar{v}\Delta\frac{\partial T'}{\partial y}$. We found that $-\bar{v}\Delta\frac{\partial T'}{\partial y}$ is the main factor causing the variation in Δ MH. Lastly, as the direction of the meridional flow is always off-equatorial, the positive and negative conversions in the MH difference are due to the variation in the meridional gradient of the SSTAs ($\Delta\frac{\partial T'}{\partial y}$).

DATA AVAILABILITY

CMIP6 model data can be downloaded from <https://esgf-node.llnl.gov/search/cmip6/>. ERSSTv5 and HadISST data can be downloaded from <https://downloads.psl.noaa.gov/Datasets/noaa.ersst.v5/> and <https://www.metoffice.gov.uk/hadobs/hadisst/data/download.html>, respectively. Additionally, FIO-ESM v2.0 data used in this study, are available from <https://doi.org/10.6084/m9.figshare.21509916.v1>.

CODE AVAILABILITY

The source code for FIO-ESM v2.0 will be provided upon request to replicate the data described in this paper. Also, the code may be requested from the corresponding author via email.

Received: 4 March 2023; Accepted: 17 September 2023;

Published online: 30 September 2023

REFERENCES

- Philander, S. El Niño southern oscillation phenomena. *Nature* **302**, 295–301 (1983).
- Alexander, M. A. et al. The atmospheric bridge: The influence of ENSO teleconnections on air-sea interaction over the global oceans. *J. Clim.* **15**, 2205–2231 (2002).
- McPhaden, M. J., Zebiak, S. E. & Glantz, M. H. ENSO as an integrating concept in earth science. *Science* **314**, 1740–1745 (2006).
- Wang, C. & Picaut, J. (eds. Wang, C., Xie, S. P. & Carton, J. A.) 21–48 (American Geophysical Union, Washington, D. C., 2004).
- Chen, X., Liao, H., Lei, X., Bao, Y. & Song, Z. Analysis of ENSO simulation biases in FIO-ESM version 1.0. *Clim. Dyn.* **53**, 6933–6946 (2019).
- Bellenger, H., Guilyardi, E., Leloup, J., Lengaigne, M. & Vialard, J. ENSO representation in climate models: from CMIP3 to CMIP5. *Clim. Dyn.* **42**, 1999–2018 (2014).
- Planton, Y. Y. et al. Evaluating climate models with the CLIVAR 2020 ENSO Metrics Package. *B. Am. Meteorol. Soc.* **102**, 193–217 (2021).
- Yan, B. & Wu, R. Relative Roles of different components of the basic state in the phase locking of El Niño Mature Phases. *J. Clim.* **20**, 4267–4277 (2007).
- Liao, H., Wang, C. & Song, Z. ENSO phase-locking biases from the CMIP5 to CMIP6 models and a possible explanation. *Deep-Sea Res. Pt. II* **189–190**, 104943 (2021).
- Jin, E. K. & Kinter, J. L. III Characteristics of tropical Pacific SST predictability in different GCM forecasts using the NCEP CFS. *Clim. Dyn.* **32**, 675–691 (2009).
- Cai, W. et al. Pan-tropical climate interactions. *Science* **363**, eaav4236 (2019).
- Brönnimann, S. et al. Extreme climate of the global troposphere and stratosphere in 1940–42 related to El Niño. *Nature* **431**, 971–974 (2004).
- Masson, S. et al. Impact of intra-daily SST variability on ENSO characteristics in a coupled model. *Clim. Dyn.* **39**, 681–707 (2012).
- Ham, Y., Kug, J., Kang, I., Jin, F. & Timmermann, A. Impact of diurnal atmosphere–ocean coupling on tropical climate simulations using a coupled GCM. *Clim. Dyn.* **34**, 905–917 (2010).
- Danabasoglu, G. et al. Diurnal coupling in the tropical oceans of CCSM3. *J. Clim.* **19**, 2347–2365 (2006).
- Tian, F., Storch, J. V. & Hertwig, E. Impact of SST diurnal cycle on ENSO asymmetry. *Clim. Dyn.* **52**, 2399–2411 (2018).
- Fairall, C. W. et al. Cool-skin and warm-layer effects on sea surface temperature. *J. Geophys. Res. Oceans* **101**, 1295–1308 (1996).
- Soloviev, A. & Lukas, R. Observation of large diurnal warming events in the near-surface layer of the western equatorial Pacific warm pool. *Deep-Sea Res. Pt. I* **44**, 1055–1076 (1997).
- Gentemann, C. L., Minnett, P. J., Le Borgne, P. & Merchant, C. J. Multi-satellite measurements of large diurnal warming events. *Geophys. Res. Lett.* **35**, L22602 (2008).
- Bernie, D. J., Woolnough, S. J., Slingo, J. M. & Guilyardi, E. Modeling diurnal and intraseasonal variability of the ocean mixed layer. *J. Clim.* **18**, 1190–1202 (2005).
- Ge, X., Wang, W., Kumar, A. & Zhang, Y. Importance of the vertical resolution in simulating SST diurnal and intraseasonal variability in an Oceanic General Circulation Model. *J. Clim.* **30**, 3963–3978 (2017).
- Yang, X., Song, Z., Tseng, Y., Qiao, F. & Shu, Q. Evaluation of three temperature profiles of a sublayer scheme to simulate SST diurnal cycle in a global ocean general circulation model. *J. Adv. Model. Earth. Sys.* **9**, 1994–2006 (2017).
- Large, W. G. & Caron, J. M. Diurnal cycling of sea surface temperature, salinity, and current in the CESM coupled climate model. *J. Geophys. Res. -Oceans* **120**, 3711–3729 (2015).
- Bao, Y., Song, Z. & Qiao, F. FIO-ESM Version 2.0: Model description and evaluation. *J. Geophys. Res.-Oceans* **125**, e2019JC016036 (2020).
- Yang, X., Song, Z. et al. Impact of resolving the diurnal cycle in an ocean-atmosphere GCM. Part 2: a diurnally coupled CGCM. *Clim. Dyn.* **31**, 909–925 (2008).
- Rayner, N. A. Global analyses of sea surface temperature, sea ice, and night marine air temperature since the late nineteenth century. *J. Geophys. Res.* **108**. <https://doi.org/10.1029/2002JD002670> (2003).
- Huang, B., Thorne, P. W., Banzon, V. F., Boyer, T. & Zhang, H. M. Extended reconstructed sea surface temperature, Version 5 (ERSSTv5): upgrades, validations, and intercomparisons. *J. Clim.* **30**. <https://doi.org/10.1175/JCLI-D-16-0836.1> (2017).
- Chen, H. & Jin, F. Fundamental behavior of ENSO phase locking. *J. Clim.* **33**, 1953–1968 (2020).
- Chen, H. & Jin, F. Simulations of ENSO phase-locking in CMIP5 and CMIP6. *J. Clim.* **34**, 5135–5149 (2021).
- Chen, H. C. & Jin, F. F. Dynamics of ENSO phase-locking and its biases in climate models. *Geophys. Res. Lett.* **49**, e2021GL097603 (2022).
- Bjerknes, J. Atmospheric teleconnections from the equatorial Pacific. *Mon. Weather Rev.* **97**, 163–172 (1969).
- Sverdrup, H. U. Wind-driven currents in a baroclinic ocean; with application to the equatorial currents of the Eastern Pacific. *P. Natl Acad. Sci. USA* **33**, 318–326 (1947).
- Li, X., Ling, T., Zhang, Y. & Zhou, Q. A 31-year global diurnal sea surface temperature dataset created by an ocean mixed-layer model. *Adv. Atmos. Sci.* **35**, 1443–1454 (2018).
- Yang, X., Song, Y., Wei, M., Xue, Y. & Song, Z. Different influencing mechanisms of two ENSO types on the interannual variation in diurnal SST over the Niño-3 and Niño-4 Regions. *J. Clim.* **35**, 125–139 (2022).
- Eyring, V. et al. Overview of the Coupled Model Intercomparison Project Phase 6 (CMIP6) experimental design and organization. *Geosci. Model Dev.* **9**, 1937–1958 (2016).

36. Guan, C. & McPhaden, M. J. Ocean processes affecting the twenty-first-century shift in ENSO SST variability. *J. Clim.* **29**, 6861–6879 (2016).

ACKNOWLEDGEMENTS

This study was supported by the National Key R&D Program of China (2022YFF0802001), the Basic Scientific Fund for the National Public Research Institutes of China (2022Q08), the National Natural Science Foundation of China (42376033, 42022042, 41821004), and the China–Korea Cooperation Project on Northwest Pacific Marine Ecosystem Simulation under Climate Change. We acknowledge the World Climate Research Programme, which, through its Working Group on Coupled Modelling, coordinated and promoted CMP6.

AUTHOR CONTRIBUTIONS

X.Y.: Investigation, Visualization, Writing-Original draft, Reviewing, Editing. Y.B.: Methodology, Data, Reviewing, Editing. Z.S.: Conceptualization, Investigation, Visualization, Analysis, Reviewing, Editing, Supervision. Q.S.: Methodology, Data, Reviewing, Editing. Y.S.: Methodology, Data, Reviewing, Editing. X.W.: Conceptualization, Reviewing, Editing, Visualization. F.Q.: Conceptualization, Reviewing, Editing, Supervision.

COMPETING INTERESTS

The authors declare no competing interests.

ADDITIONAL INFORMATION

Supplementary information The online version contains supplementary material available at <https://doi.org/10.1038/s41612-023-00483-3>.

Correspondence and requests for materials should be addressed to Zhenya Song, Xin Wang or Fangli Qiao.

Reprints and permission information is available at <http://www.nature.com/reprints>

Publisher's note Springer Nature remains neutral with regard to jurisdictional claims in published maps and institutional affiliations.



Open Access This article is licensed under a Creative Commons Attribution 4.0 International License, which permits use, sharing, adaptation, distribution and reproduction in any medium or format, as long as you give appropriate credit to the original author(s) and the source, provide a link to the Creative Commons license, and indicate if changes were made. The images or other third party material in this article are included in the article's Creative Commons license, unless indicated otherwise in a credit line to the material. If material is not included in the article's Creative Commons license and your intended use is not permitted by statutory regulation or exceeds the permitted use, you will need to obtain permission directly from the copyright holder. To view a copy of this license, visit <http://creativecommons.org/licenses/by/4.0/>.

© The Author(s) 2023